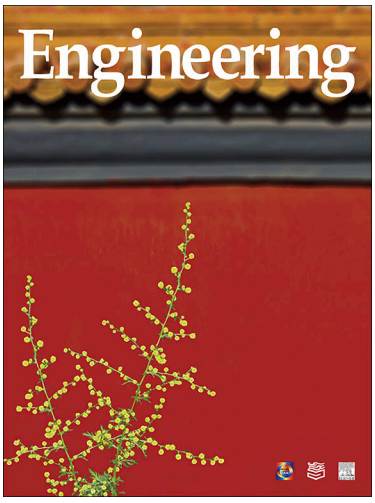
Journal Pre-proofs



Article

Global Terrestrial Photosynthesis Increased Substantially During 2000–2023, Driven by Changing Atmospheric CO_2 Concentration, Climate, and Vegetation

Li Pan, Xiangming Xiao, Cheng Meng, Baihong Pan, Shenglai Yin, Chenchen Zhang, Yuan Yao, Yuanwei Qin

PII: S2095-8099(26)00564-3
DOI: https://doi.org/10.1016/j.eng.2026.09.014
Reference: ENG 2478

To appear in: *Engineering*

Received Date: 14 September 2025
Revised Date: 5 August 2026
Accepted Date: 3 September 2026

Please cite this article as: L. Pan, X. Xiao, C. Meng, B. Pan, S. Yin, C. Zhang, Y. Yao, Y. Qin, Global Terrestrial Photosynthesis Increased Substantially During 2000–2023, Driven by Changing Atmospheric CO_2 Concentration, Climate, and Vegetation, *Engineering* (2026), doi: https://doi.org/10.1016/j.eng.2026.09.014

This is a PDF of an article that has undergone enhancements after acceptance, such as the addition of a cover page and metadata, and formatting for readability. This version will undergo additional copyediting, typesetting and review before it is published in its final form. As such, this version is no longer the Accepted Manuscript, but it is not yet the definitive Version of Record; we are providing this early version to give early visibility of the article. Please note that Elsevier's sharing policy for the Published Journal Article applies to this version, see: https://www.elsevier.com/about/policies-and-standards/sharing#4-published-journal-article. Please also note that, during the production process, errors may be discovered which could affect the content, and all legal disclaimers that apply to the journal pertain.

© 2026 THE AUTHORS. Published by Elsevier LTD on behalf of Chinese Academy of Engineering and Higher Education Press Limited Company

Research
Climate and Sustainable Engineering—Article

Global Terrestrial Photosynthesis Increased Substantially During 2000–2023, Driven by Changing Atmospheric CO_2 Concentration, Climate, and Vegetation

Li Pan [a], Xiangming Xiao [a,*], Cheng Meng [a], Baihong Pan [a], Shenglai Yin [a], Chenchen Zhang [a], Yuan Yao [a], Yuanwei Qin [b]

[a] *School of Biological Sciences, University of Oklahoma, Norman, OK 73019, USA*

[b] *Jiangsu Key Laboratory of Soil and Water Processes in Watershed, College of Geography and Remote Sensing, Hohai University, Nanjing 211100, China*

*Corresponding author.
E-mail address: xiangming.xiao@ou.edu (X. Xiao).

Article Infor

Received

Revised

Accepted

Available online

Keywords

Gross primary production

Climate change

Light use efficiency

Remote sensing

CO_2 concentration

ABSTRACT

Modeling and prediction of terrestrial gross primary production (GPP) in the globe face many challenges. Here we use the Vegetation Photosynthesis Model (VPM-v4), satellite images, atmospheric CO_2 concentration data, ERA5-Land dataset, and annual land cover maps to estimate global GPP during 2000–2023. At the site scale, annual GPP and its interannual variability (IAV), and the trends from VPM-v4 have strong agreement with those from the eddy covariance tower sites that have ≥ 10 years of measurements, a total of 777 site-years. At the global scale, global annual GPP estimate from VPM-v4 varies from 145 petagrams of carbon per year (Pg $C \cdot a^{-1}$) in 2000 to 166 Pg $C \cdot a^{-1}$ in 2023, with an increasing trend of 0.78 Pg $C \cdot a^{-2}$, which is higher than that from most terrestrial biospheric models (TBMs) and Earth system models (ESMs). The biochemical CO_2 effect on annual GPP varies among the biomes and is high in tropical and subtropical forests and contributes substantially to continued increase of global annual GPP during 2000–2023. In comparison to many TBMs and ESMs, global GPP estimates from VPM-v4 falls within the range of annual GPP estimates from carbonyl sulfide (OCS)-based method (157 Pg $C \cdot a^{-1}$; 2000–2010), respiration-based method (149 Pg $C \cdot a^{-1}$), and ^{18}O-based method (150–175 Pg $C \cdot a^{-1}$). By integrating a Farquhar–von Caemmerer–Berry model (FvCB)-based representation of the biochemical CO_2 effect into a scalable satellite-based light use efficiency (LUE) framework, this study bridges biochemical photosynthesis theory and global remote-sensing observations, advances the

assessment of long-term GPP change, and provides a complementary basis for terrestrial carbon-cycle studies and TBM/ESM evaluation.

1. Introduction

Terrestrial gross primary production (GPP) is the largest carbon flux in the global carbon cycle [1–3]. Accurately quantifying GPP is essential for understanding how terrestrial ecosystems respond to and regulate the impacts of climate change and rising atmospheric CO_2, as well as for formulating practices and policies for the management and conservation of these ecosystems [4,5]. Many prognostic and diagnostic terrestrial biospheric models (TBMs) and Earth system models (ESMs) have been developed and applied to estimate global GPP over the years, and these models vary in terms of model processes, variables, algorithms, and parameters, ranging from complex and prognostic TBMs/ESMs incorporating detailed physiological processes (e.g., dynamic global vegetation models (DGVMs)) to simple, diagnostic, data-driven models that combine remote sensing data and statistical methods [6–11]. Over the past several decades, the estimates of global annual GPP from many models were approximately ~120 petagrams of carbon per year (Pg $C \cdot a^{-1}$) [3], which has been widely used in the study of the global carbon cycle and budgets. However, recent studies reported that global annual GPP could be as high as ~(157 ± 8.5) Pg $C \cdot a^{-1}$ using the carbonyl sulfide (OCS) flux method [12], ~149 Pg $C \cdot a^{-1}$ with a soil respiration method [13], and 150–175 Pg $C \cdot a^{-1}$ using the ^{18}O method [14]. Given the large discrepancies among these GPP estimates and the role of GPP in the carbon cycle, further development in GPP modeling is needed.

Plant photosynthesis is composed of light absorption (L), electron transport (J), and CO_2 assimilation (A) (Calvin cycle) processes [15,16], which are represented differently in TBMs and ESMs. According to the classic Farquhar–von Caemmerer–Berry model (FvCB) biochemical model of photosynthesis, which uses the maximum rate of RuBisCo carboxylase activity (Vc_{max}) as a key parameter, higher atmospheric CO_2 concentration (c_a) increases the CO_2 supply within leaves (c_i), which could lead to a higher proportion of Rubisco carboxylation (CO_2 fixation or assimilation) and a lower proportion of Rubisco oxygenation (photorespiration), thereby directly improving photosynthetic efficiency [16–18]. This "biochemical CO_2 effect" on GPP is theoretically critical [19]. Among the data-driven TBMs, one group of models explicitly calculates light absorption and uses light use efficiency (LUE) to approximate the complex CO_2 assimilation process [6]. The basic assumption of the LUE models is that photosynthesis is directly related to absorbed photosynthetically active radiation (APAR) and LUE (ε_g). ε_g is a parameter related to the maximum LUE (ε_{max}), which represents the theoretical ε_{max} that vegetation can attain under stress-free or optimal growth conditions [6,20]. Multiple environmental factors, such as air temperature, water availability (e.g., vapor pressure deficit (VPD), soil moisture, and leaf water content), and c_a, are used to constrain or downregulate ε_{max} and calculate the actual LUE (ε_g) under prevailing environmental conditions. It is important to note that most LUE models do not explicitly account for the effect of c_a on ε_{max}. Due to the absence of an explicit representation of the biochemical CO_2 effect, many LUE models may systematically underestimate GPP [2,21]. Global annual GPP estimates from these LUE models are in the range of 120–140 Pg $C \cdot a^{-1}$ [3,22–24]. Underestimation of GPP is particularly severe in high-productivity regions such as pan-tropical rainforests [12,25]. Since the biochemical CO_2 effect often interacts with air temperature and photosynthetically active radiation (PAR) conditions [17,19], failing to incorporate it into LUE models explicitly may be closely linked to this underestimation of GPP. It is important to note that these models do consider the "biophysical CO_2 effect," whereby higher c_a leads to greater leaf area or vegetative cover over time, allowing plants to intercept more PAR—a biophysical process [26,27]. As these LUE models use leaf area index (LAI) or vegetation indices derived from satellite data to estimate light absorption, they can capture the biophysical CO_2 effect but lack an explicit representation of the biochemical CO_2 effect.

In addition to the magnitudes of global annual GPP estimates from these models, a large range and considerable uncertainty also persist in the interannual variability (IAV) and trends of global annual GPP estimates from the LUE models [1,2]. A review of multiple satellite-based GPP products indicates that the LUE models without the biochemical CO_2 effect (e.g., Model Tree Ensemble (MTE) and Moderate Resolution Imaging Spectroradiometer (MODIS)) show weaker IAV and trends than most process-based models [2]. Recent work suggests that rising c_a explains approximately 44% of the global GPP increase over years [17], with about 13.5% contributed by the biochemical CO_2 effect [19]. This implies that at least one-third of the GPP increase is underestimated by current LUE models [17]. Moreover, different GPP data products vary substantially in their sensitivities to the biochemical CO_2 effect [28,29], and these sensitivities remain underestimated [2,19,30]. Current improvements to LUE models have primarily focused on refining model parameters and environmental constraints [31,32], with few studies systematically incorporating the biochemical CO_2 effect as an independent factor [33].

In this study, we develop the new version of the Vegetation Photosynthesis Model (VPM-v4), which is built upon a previous version (VPM-v3) [31,32,34] and explicitly incorporates the biochemical CO_2 effect based on the FvCB biochemical photosynthetic CO_2 assimilation theory [16]. We hypothesize that explicit incorporation of the biochemical CO_2 effect improves VPM's model performance in estimating GPP and its IAV and trend. The VPM-v4 explicitly considers ① light absorption by chlorophyll and leaf traits (broad leaf or flat leaf vs needle leaf); ② CO_2 assimilation by plant functional types (C_3 and C_4 plants); and ③ the effects of air temperature, water, and c_a on CO_2 assimilation. Through simulations of VPM-v4 and VPM-v3, driven by c_a, ERA5-Land climate data, annual land cover maps, and satellite images, we have three specific objectives in this study.

First, we assessed the biochemical CO_2 effect on GPP at the scale of eddy covariance (EC) tower sites. We achieved this by comparing annual GPP and its IAV and trends from VPM-v4, VPM-v3, and EC observations. Second, we calculated global annual GPP during 2000 – 2023 from VPM-v4 and VPM-v3 and assessed the biochemical CO_2 effect on GPP at the global scale. Third, we compared the global annual GPP, IAV, trends, and their sensitivity to CO_2 (β_R^{GPP}) between VPM-v4, VPM-v3, and other models. VPM-v4 may reduce the systematic underestimation of global GPP that is common in many LUE models, particularly in highly productive tropical regions, and provides a more realistic representation of the IAV and long-term trends of annual GPP. The resulting global GPP dataset could provide useful data for assessing GPP's sensitivity to atmospheric CO_2 and evaluating the performance of more complex TBMs and ESMs.

2. Material and methods

2.1. MOD09A1 v6.1 surface reflectance dataset

MOD09A1 v6.1 provides surface reflectance data for seven spectral bands at a 500-m spatial resolution and an 8-d temporal resolution. The data product is corrected for atmospheric effects such as gases, aerosols, and Rayleigh scattering [35]. We preprocessed the surface reflectance data by removing observations flagged by quality assurance (QA) as contaminated by clouds, snow, or cloud shadows [36], and applying a blue-band threshold of 0.2 to filter out residual noise caused by atmospheric scattering [37]. In addition, we performed temporal consistency check by using a 3-observation moving window ($t-1$, t, $t+1$) to eliminate abrupt reflectance changes inconsistent with normal vegetation dynamics [31]. Specifically, if the absolute slope between the middle and adjacent time steps exceeded 0.15, we deemed the observation anomalous (i.e., of poor quality) and removed it. Enhanced vegetation index (EVI) and the land surface water index (LSWI) were then calculated as inputs to the VPMs, defined respectively as

$$\mathrm{EVI} = 2.5 \times \frac{\rho_{\mathrm{nir}} - \rho_{\mathrm{red}}}{\rho_{\mathrm{nir}} + (6 \times \rho_{\mathrm{red}} - 7.5 \times \rho_{\mathrm{blue}}) + 1} \quad (1)$$

$$\mathrm{LSWI} = \frac{\rho_{\mathrm{nir}} - \rho_{\mathrm{swir}}}{\rho_{\mathrm{nir}} + \rho_{\mathrm{swir}}} \quad (2)$$

where ρ_{nir}, ρ_{red}, ρ_{blue}, and ρ_{swir} are the surface reflectance bands of near-infrared, red, blue, and shortwave-infrared, respectively. Here, we applied the surface reference curves from multi-year high quality observations and linear interpolation to fill the data gaps in the vegetation index time series [23,32].

2.2. MCD12Q1 v6.1 land cover type dataset

MCD12Q1 v6.1 provides 500-m global land cover classification layers, generated by machine learning algorithms and time-series smoothing techniques [38]. In this study, we employed the land cover types identified by the International Geosphere-Biosphere Programme (IGBP) and focused on the following 11 categories: croplands (CRO), closed shrublands (CSH), deciduous broadleaf forests (DBF), evergreen broadleaf forests (EBF), evergreen needleleaf forests (ENF), grasslands (GRA), mixed forests (MF), open shrublands (OSH), savannas (SAV), permanent wetlands (WET), and woody savannas (WSA).

2.3. ERA5-Land reanalysis climate dataset

The ERA5-Land reanalysis climate dataset, developed by the European Centre for Medium-Range Weather Forecasts (ECMWF) [39,40], provides land surface variables at 0.1° spatial resolution and an hourly temporal resolution, allowing for a refined representation of local climate conditions and their short-term fluctuations. A previous study comparing ground-based climate measurements at 205 global EC tower sites with the ERA5-Land data showed strong agreement [32]. In this study, we selected air temperature (T) and shortwave radiation (SW) from ERA5-Land as model inputs. SW ($W \cdot m^{-2}$) was first converted to PAR expressed as energy (PARE, $W \cdot m^{-2}$), and then to PAR expressed as photosynthetic photon flux density (PPFD, $\mu mol \cdot m^{-2} \cdot s^{-1}$), as follows:

$$\mathrm{PPFD} = \mathrm{SW} \times r_{\mathrm{SW_PAR}} \times \alpha \quad (3)$$

where $r_{\mathrm{SW_PAR}} = 0.45$ is the conversion coefficient from SW ($W \cdot m^{-2}$) to PARE ($W \cdot m^{-2}$) [31,32,41,42], and $\alpha = 4.56$ $\mu mol \cdot J^{-1}$ is the conversion coefficient between energy (PARE, $W \cdot m^{-2}$) and quanta (PPFD, $\mu mol \cdot m^{-2} \cdot s^{-1}$) [31,32,43].

In addition, we calculated the VPD from air temperature (T) and dew point temperature (T_d) using

$$\mathrm{VPD} = 0.6108 \times \exp\left(\frac{17.27T}{T + 237.3\ ^\circ\mathrm{C}}\right) - 0.6108 \times \exp\left(\frac{17.27T_d}{T_d + 237.3\ ^\circ\mathrm{C}}\right) \quad (4)$$

2.4. Atmospheric CO_2 concentration

The annual c_a dataset is from the National Oceanic and Atmospheric Administration (NOAA). Based on globally averaged marine surface measurements from multiple monitoring stations, this dataset captures long-term variations in atmospheric CO_2 levels. We obtained annual c_a spanning from 2000 to 2023 from Ref. [44].

2.5. Global multi-resolution terrain elevation dataset

The Global Multi-resolution Terrain Elevation Data 2010 (GMTED2010) dataset provides globally distributed elevation data at approximately 250-m spatial resolution, compiled from multiple sources [45]. The primary data source for GMTED2010 is the National Geospatial-Intelligence Agency's (NGA) Shuttle Radar Topography Mission (SRTM) Digital Terrain Elevation Data.

2.6. In-situ *carbon flux data from the EC tower sites*

We used *in-situ* GPP data from the EC tower sites to compare predicted GPP from VPM simulations. The *in-situ* GPP site data were obtained from AmeriFlux and the FLUXNET portals. To evaluate GPP IAV, we selected sites with at least 10 years of observations (site-year ≥ 10) and high data quality (i.e., > 90% high-quality observations labeled by quality flag). We further restricted sites to latitudes between 60°N and 60°S. We also compared the IGBP ecosystem classifications provided by FLUXNET2015 or AmeriFlux with those from the MODIS land cover data product, excluding any sites with mismatched classifications. After screening, 59 sites were retained, spanning 11 biome types and totaling 777 site-years. Detailed IGBP ecosystem classifications and data availability for these sites are provided in Fig. S1 in Appendix A.

2.7. GPP datasets from other models

For GPP comparison, we selected multiple global GPP estimates derived from various models. These models are grouped by their methods. The first group includes the OCS-based estimates [12], the oxygen isotope (^{18}O)-based estimates [14], and soil respiration-based estimates [13]. The second group includes 13 DGVMs, from version 13 of the Trends and Drivers of Terrestrial Sources and Sinks of Carbon Dioxide used for the Global Carbon Budget 2024 (TRENDY–GCB2024), which encompass CO_2-inclusive scenario (S2) as well as CO_2-exclusive scenario (S2 − S1 + S0; where S1 represents the simulation with varying atmospheric CO_2 under baseline climate and land-use conditions, and S0 represents the baseline simulation with fixed pre-industrial CO_2 and land-use conditions [46]) (Text S1 in Appendix A). The third group includes the Photosynthesis and Respiration (PR) Model, the Breathing Earth System Simulator (BESS), and the Biosphere–Atmosphere Exchange Process Simulator (BEPS) models, which simulate ecophysiological processes to estimate GPP [10,11,47]. The fourth group includes the simple statistical models using remote sensing data (e.g., Global OCO-2 Solar-Induced Chlorophyll Fluorescence (GOSIF) and Near-Infrared Reflectance of Vegetation (NIRv)), which rely on the statistical relationships between SIF or vegetation indices and *in-situ* GPP to estimate GPP [24,48]. The fifth group includes the machine learning models using remote sensing and climate data (e.g., the Global Land Carbon Fluxes dataset from FLUXCOM RS+METEO, which uses CRUNCEP climate data), which combines *in-situ* GPP data, remote sensing data, and CRUNCEP climate data for GPP estimation [7,49]. The sixth group includes the LUE models, including the newly developed VPM-v4 (with CO_2) in this study, VPM-v3 (without CO_2), Global Land Surface Satellite (GLASS), EC-LUE, Light Response Function (LRF), and the MODIS MOD17 GPP/ net primary production (NPP) product (MOD17) [50–53]. Additional details and corresponding citations can be found in Tables S1 and S2 in Appendix A.

2.8. Incorporating biochemical effect of CO_2 on GPP into the VPMs

VPM estimates daily GPP (g $C \cdot m^{-2} \cdot d^{-1}$) and considers two processes: ① the light absorption process (i.e., light absorption by chlorophyll ($APAR_{chl}$ = PPFD × $FPAR_{chl}$), and ② the CO_2 assimilation process (i.e., LUE (ε_g)). In VPM-v3, we consider air temperature and water to downregulate the maximum LUE (ε_{max}) ($\varepsilon_g = \varepsilon_{max} \times f(T) \times f(W)$):

$$GPP_{VPM}\text{-v3} = PPFD \times FPAR_{chl} \times \varepsilon_{max} \times f(T) \times f(W) \quad (5)$$

$$FPAR_{chl} = \begin{cases} a + \gamma_E \times EVI, & \text{if needleleaf} \\ a + EVI, & \text{if broadleaf} \end{cases} \quad (6)$$

$$f(T) = \frac{(T - T_{max}) \times (T - T_{min})}{(T - T_{max}) \times (T - T_{min}) - (T - T_{opt})^2} \quad (7)$$

$$f(W) = \frac{1+\mathrm{LSWI}}{1+\mathrm{LSWI}_{\max}} \quad (8)$$

where $\mathrm{FPAR}_{\mathrm{chl}}$ is calculated as a linear function of EVI, with the coefficient a set to −0.1. γ_{E} represents needleleaf trait related to how chloroplasts are arranged in needleleaf. Here γ_{E} is a leaf structure correction factor, introduced in VPM-v3 to reduce the underestimation of $\mathrm{APAR}_{\mathrm{chl}}$ in needleleaf (γ_{E} = 1.25) [32]. The apparent quantum yield, or maximum LUE, $\varepsilon_{\max}$ is set at 0.53 (g $\mathrm{C}\cdot(\mathrm{mol\ PAR})^{-1}$ or 0.044 mol $\mathrm{CO_2}\cdot(\mathrm{mol\ PAR})^{-1}$) for $\mathrm{C_3}$ plants and 0.79 (g $\mathrm{C}\cdot(\mathrm{mol\ PAR})^{-1}$ or 0.066 mol $\mathrm{CO_2}\cdot(\mathrm{mol\ PAR})^{-1}$) for $\mathrm{C_4}$ plants, and for mixed $\mathrm{C_3}$ – $\mathrm{C_4}$ pixels we use a fractional-cover-weighted average $\varepsilon_{\max}$ [32,54]. $f(T)$ and $f(W)$ are the dimensionless temperature and water stress scalars, respectively. The air temperature parameters $T_{\min}$, T_{opt}, and $T_{\max}$ are the minimum, optimum, and maximum temperatures for $\mathrm{CO_2}$ assimilation, respectively. $T_{\max}$ and $T_{\min}$ were obtained from a look-up table for individual biomes, and T_{opt} was obtained from a global site-specific T_{opt} dataset [55]. Previous studies have shown that site-specific T_{opt} improves characterization of $\mathrm{CO_2}$ assimilation response curve to air temperature and model performance [32]. EVI and LSWI were calculated from MOD09A1 multispectral surface reflectance data.

In VPM-v4, we consider the biochemical effect of c_{a} on $\mathrm{CO_2}$ assimilation. Previous studies have demonstrated that the sensitivity of ecosystem-scale GPP to $\mathrm{CO_2}$ is consistent with the sensitivity of electron transport-limited gross photosynthetic rate (A_{gross}) [19,56]. Hence, the influence of $\mathrm{CO_2}$ on $\mathrm{CO_2}$ assimilation can be incorporated into the VPM as an additional environmental factor. VPM-v4 estimates daily GPP as

$$\mathrm{GPP_{VPM}\text{-}v4} = \mathrm{PPFD} \times \mathrm{FPAR_{chl}} \times \varepsilon_{\max} \times f(T) \times f(W) \times f(\mathrm{CO_2}) \quad (9)$$

Note that $f(\mathrm{CO_2})$ is applied only to $\mathrm{C_3}$ plants. $f(\mathrm{CO_2})$ can be estimated through the following steps. To highlight that the biochemical $\mathrm{CO_2}$ effect is "additional" or relative to pre-industrial levels, we establish a baseline assumption that pre-industrial c_{a} were maintained at a relatively stable and low value. As c_{a} increased over time, the model compares simulation results between two $\mathrm{CO_2}$ scenarios (or different observation years) to quantify the additional carbon fixed at the biochemical level in the leaves. Thus, $f(\mathrm{CO_2})$ is quantified as a relative gain compared to the pre-industrial era:

$$f(\mathrm{CO_2}) = \frac{\mathrm{A}_{\mathrm{gross}}^{t}}{\mathrm{A}_{\mathrm{gross}}^{\mathrm{baseline}}} \quad (10)$$

where A_{gross} is estimated according to the biochemical photosynthetic $\mathrm{CO_2}$ assimilation theory in the FvCB model (Text S2 in Appendix A). t denotes the simulation year from 2000 to 2023. In this study, we estimate the pre-industrial baseline ($\mathrm{A}_{\mathrm{gross}}^{\mathrm{baseline}}$) using c_{a} = 278 ppm and reference climatology based on ERA5-Land data from 1950s [57]. Because gridded climate fields for year 1750 are not available, we conducted a sensitivity analysis in which the 1951–1960 baseline climate was perturbed to construct three synthetic climate scenarios representative of pre-industrial conditions. The resulting $f(\mathrm{CO_2})$ fields differ from the original baseline by less than 1% globally (Fig. S2 in Appendix A), indicating that using the 1950s climate as a baseline is within an acceptable error range. Accordingly, our $\mathrm{CO_2}$-related estimate represents an effective net $\mathrm{CO_2}$-related contribution under the stated assumptions, not a strict pre-industrial climate counterfactual attribution. Then, for each year from 2000 to 2023, we estimate $\mathrm{A}_{\mathrm{gross}}^{t}$ using the corresponding $\mathrm{CO_2}$ concentration and climate data. Finally, $f(\mathrm{CO_2})$ is calculated as the ratio of $\mathrm{A}_{\mathrm{gross}}^{t}$/ $\mathrm{A}_{\mathrm{gross}}^{\mathrm{baseline}}$. As a result, $f(\mathrm{CO_2})$ is a dimensionless factor defined as the relative enhancement of leaf-level photosynthesis by rising $\mathrm{CO_2}$. Our results indicate that, from a global perspective, regions with higher $f(\mathrm{CO_2})$ values are predominantly located in the low-latitude tropics and subtropics (Figs. S3(a)–(c) in Appendix A). Moreover, the long-term trend shows a significant increase in $f(\mathrm{CO_2})$ in these regions, suggesting that the biochemical $\mathrm{CO_2}$ effect is most pronounced in tropical and subtropical regions and diminishes with increasing latitudes (Fig. S3(d) in Appendix A).

3. Results

3.1. Biochemical CO_2 effect on annual GPP at the EC tower sites

At the site scale, we compared annual $\mathrm{GPP_{EC}}$ (g $\mathrm{C}\cdot\mathrm{m^{-2}}\cdot\mathrm{a^{-1}}$) from 59 EC tower sites with GPP from VPM-v4 (with $\mathrm{CO_2}$) and VPM-v3 (without $\mathrm{CO_2}$) over 777 site-years (Fig. 1). The comparison focused on annual GPP and its IAV and trends. Annual $\mathrm{GPP_{EC}}$ shows an increasing GPP trend from 2000 to 2023 with a rate of 6.0 g $\mathrm{C}\cdot\mathrm{m^{-2}}\cdot\mathrm{a^{-2}}$ (Fig. 1(a)). Annual GPP from VPM-v4 also shows an increasing GPP trend over the years with a rate of 5.3 g $\mathrm{C}\cdot\mathrm{m^{-2}}\cdot\mathrm{a^{-2}}$, which is slightly (12%) lower than that from the EC tower sites. Annual GPP from VPM-v3 did have an increasing trend, but with a much smaller rate of 3.8 g $\mathrm{C}\cdot\mathrm{m^{-2}}$ $\mathrm{a^{-2}}$. Those sites that have a higher $f(\mathrm{CO_2})$ also exhibit larger GPP IAV, and the sensitivity of GPP IAV to $f(\mathrm{CO_2})$ in VPM-v4 is closer to that from the EC tower sites than VPM-v3 (Fig. S4 in Appendix A). These results suggest that incorporation of $f(\mathrm{CO_2})$ into the VPM-v4 model enhances its ability to capture the GPP IAV and trend at the EC tower sites. This improved prediction of GPP IAV by VPM-v4 is evident across most biomes, including CRO, CSH, EBF, ENF, GRA, MF, and WSA (Fig. S5 in Appendix A).

With regard to annual GPP (g $\mathrm{C}\cdot\mathrm{m^{-2}}\cdot\mathrm{a^{-1}}$), a linear regression analysis (without an intercept, emphasizing a comparison of one variable from two methods) between VPM-v4 estimates and EC tower observations yielded a slope of 0.99, a coefficient of

determination (R^2) of 0.67, and a relative root-mean-square error (rRMSE) of 33.07% (Fig. 1(b)), higher than that from the regression analysis between VPM-v3 and EC tower observations (slope = 0.90, R^2 = 0.67, rRMSE = 34.51%) (Fig. 1(c)). The closer-to-unity (i.e., the 1:1 line) slope for VPM-v4 indicates that it does not underestimate GPP at the site scale after we incorporate the biochemical CO_2 effect on GPP. This improvement of VPM-v4 over VPM-v3 is also observed in biomes such as EBF, ENF, SAV, and CRO (Fig. S6 in Appendix A).

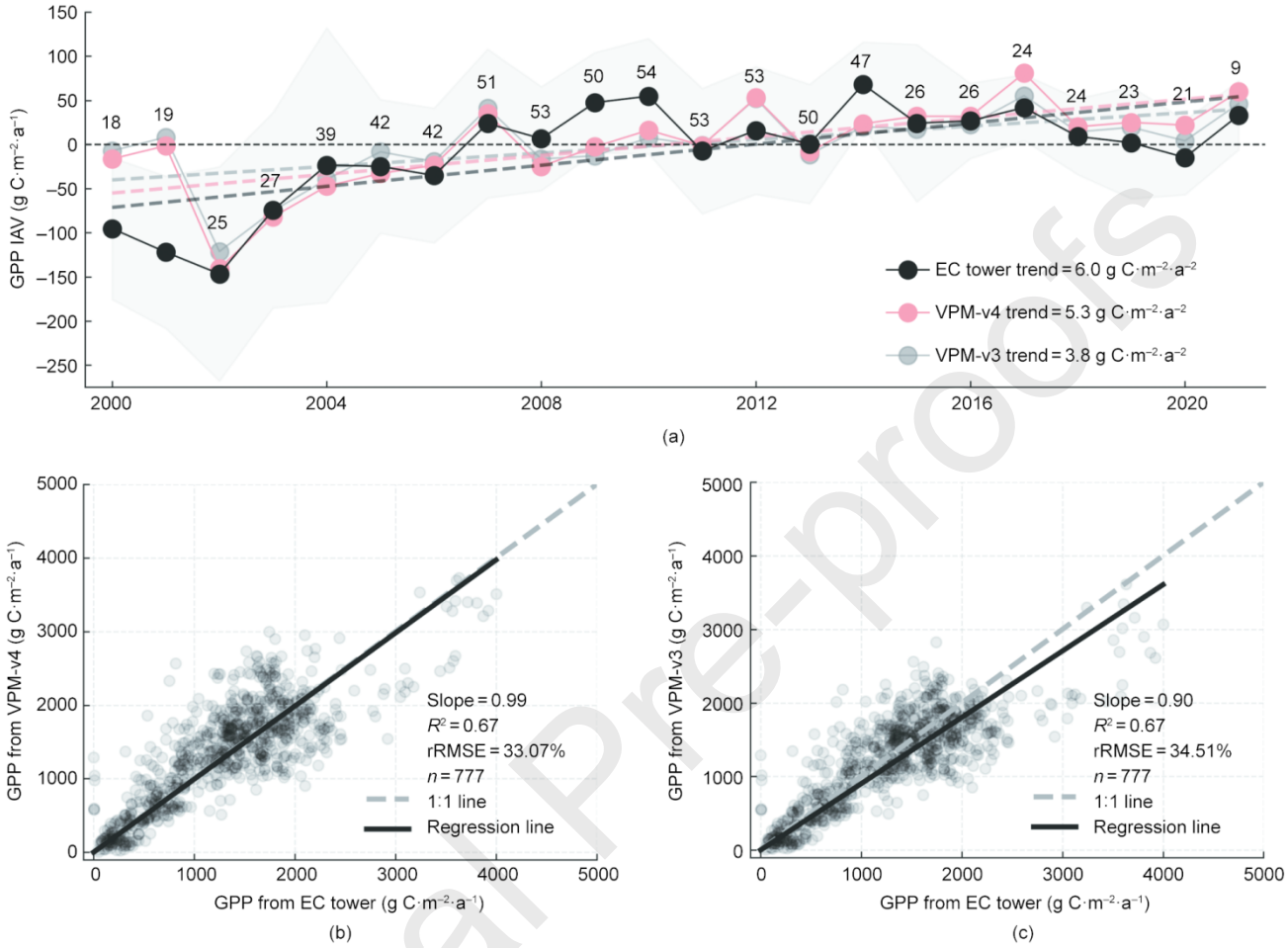


Fig. 1. Comparison of GPP estimates from EC tower measurements and the VPMs (VPM-v4 and VPM-v3). (a) Comparison of GPP IAV, where IAV was quantified as the standard deviation of annual GPP anomalies relative to the multi-year mean. Each point in the time series represents the mean GPP IAV across all site-years, with the number annotated on each point indicating the total number of site-years for that year from sites. The grey buffer represents the GPP range derived using covariance techniques from both nighttime- and daytime-partitioning methods. (b, c) Comparison of annual GPP magnitude, with (b) showing the relationship between GPP from VPM-v4 and EC tower, and (c) showing the relationship between GPP from VPM-v3 and EC tower. The annual GPP magnitude was calculated as the total GPP over a year, and these comparisons are conducted using simple linear regression.

3.2. Biochemical CO_2 effect on GPP at the global scale from 2000 to 2023

Global annual GPP estimates during 2000–2023 from VPM-v4 (with CO_2) range from 145 Pg C·a^{-1} in 2000 to 166 Pg C·a^{-1} in 2023, with an average estimate of (155 ± 6) Pg C·a^{-1} and an annual increase rate of 0.78 Pg C·a^{-2} (Fig. 2(a)). Global annual GPP estimates from VPM-v3 (without CO_2) range from 135 Pg C·a^{-1} in 2000 to 151 Pg C·a^{-1} in 2023, with an average estimate of (143 ± 4) Pg C·a^{-1} and an annual increase rate of 0.57 Pg C·a^{-2} (Fig. 2(a)). On average, the biochemical CO_2 effect (VPM-v4) results in an increase of mean global annual GPP (12 Pg C·a^{-1}; ~9%) over the VPM-v3. The spatial differences between these two GPP data products are most pronounced in the tropical and subtropical regions (Figs. 2(b)–(d)), where vegetation are dominated by EBF, GRA, WSA, SAV, and CRO (Figs. S7 and S8 in Appendix A). Mid-to-high latitude regions dominated by DBF, ENF, MF, and OSH exhibit relatively smaller differences (Figs. S7 and S8). At the scale of biomes (Fig. S9 in Appendix A), the largest difference between these two models occurred in EBF, where mean annual GPP from VPM-v4 was 38.46 Pg C·a^{-1}, approximately ~3.19 Pg C·a^{-1} (~9%) higher than the estimate from VPM-v3 of 35.26 Pg C·a^{-1}. Biomes such as GRA, SAV, CRO, and WSA also exhibit varying degrees of GPP increase in VPM-v4. In contrast, DBF, ENF, MF, and OSH show small differences between VPM-v4 (with CO_2) and VPM-v3 (without CO_2).

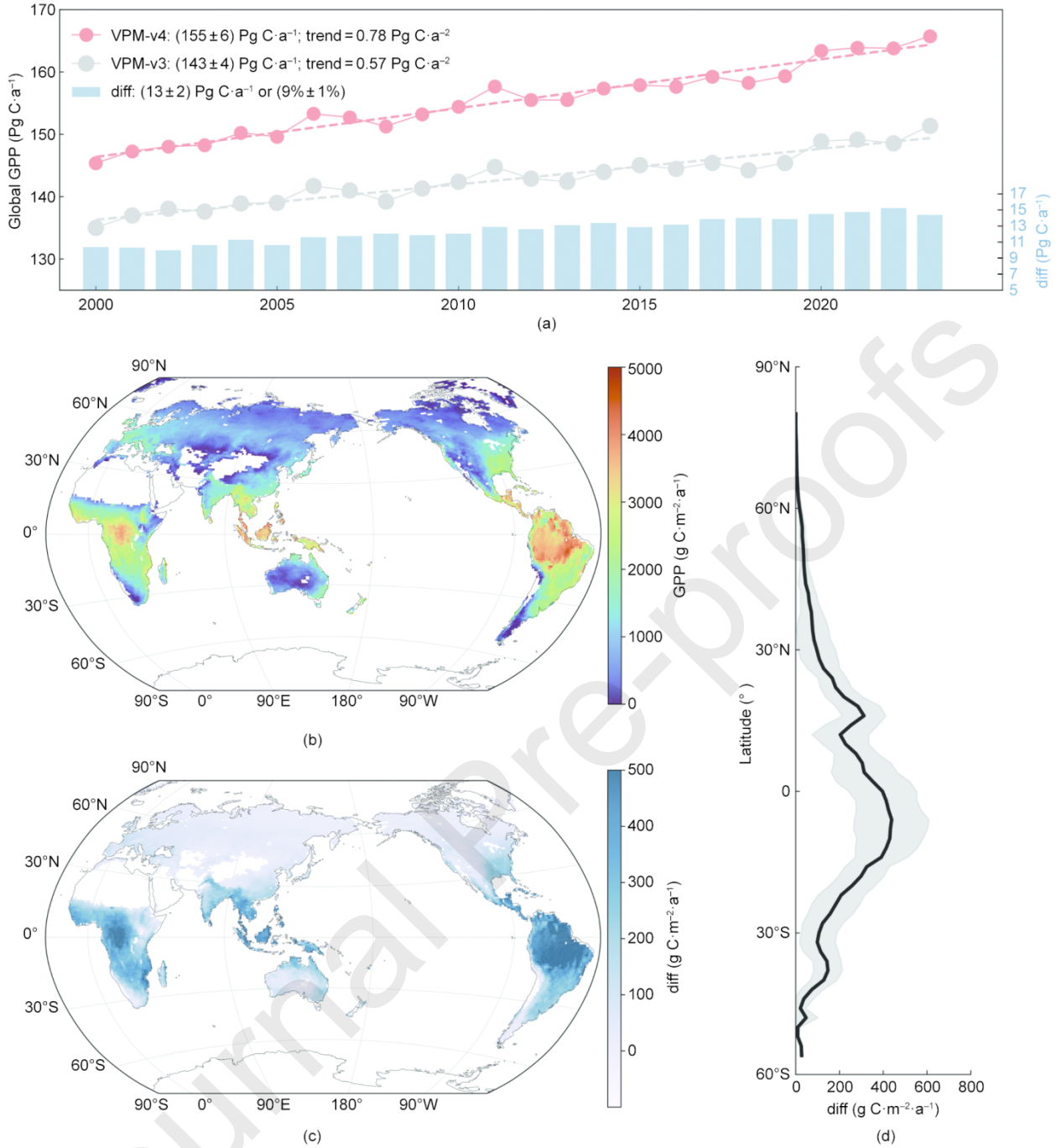


Fig. 2. Comparison of global GPP estimates from VPM-v4 and VPM-v3. (a) The global GPP estimated by VPM-v4 and VPM-v3 from 2000 to 2023, where the difference (diff) is calculated as the difference between VPM-v4 and VPM-v3. (b) The spatial distribution of the annual GPP magnitude estimated by VPM-v4, while (c) is the spatial distribution of the diff in annual GPP magnitude between VPM-v4 and VPM-v3. (d) The latitudinal gradient of the diff, with the curve representing the average of all pixels within each 2° latitudinal bands. Data analysis was carried out at a 500-m spatial resolution and visualized at a 1° spatial resolution.

3.3. Comparison of global annual GPP estimates from VPM-v4 and other GPP models

We compared the global annual GPP estimates from the VPM-v4 model with those from other models in terms of annual GPP magnitude and interannual trends. The models in the comparison are grouped into four categories: ① DGVMs, including 13 models that run simulations with CO_2 or without CO_2; ② satellite-based models using Vc_{max} parameter for CO_2 assimilation, including BESS, BEPS, and PR; ③ satellite-based model using ε_{max} parameter for CO_2 assimilation with or without biochemical CO_2 effect, including VPM-v4 and VPM-v3, MOD17, LRF, EC-LUE, and GLASS; and ④ statistical models trained with EC data and satellite data (FPAR, NIRv, and SIF), including FLUXCOM, NIRv, and GOSIF models.

As shown in Fig. 3(a), the mean global annual GPP estimate during 2000–2023 from VPM-v4 ((155 ± 6) Pg C·a^{-1}) is very close to the estimate from the OCS method ((157 ± 8.5) Pg C·a^{-1}, 2000–2010) [12], within the range of 150–175 Pg C·a^{-1} from ^{18}O methods [14], and slightly higher than the estimate of 149 Pg C·a^{-1} from soil respiration method [13]. A latitudinal profile comparison of annual GPP from VPM with that from the OCS method reveals a high degree of consistency along the latitudinal gradient (Fig. 3(b)). In the tropical regions, annual GPP from VPM-v3 is smaller than that from the OCS method, whereas annual GPP from VPM-v4 is closer to that from the OCS method. VPM-v4 GPP magnitude closely matches that from the OCS method between 0°S and 10°S latitudinal zone. Note that annual GPP from VPM-v4 between 10°S and 20°S latitudinal zone is slightly higher than that from the OCS method, where vegetation in Africa is dominated by C_4 grasses. VPM-v4 model simulations employed an updated and detailed C_4 vegetation distribution map (Section 2 for more details). Note that C_4 plants have higher maximum LUE parameter value than C_3 plants.

Mean global annual GPP estimates from various models are compared (Fig. 3, Fig. S10 in Appendix A and Table S1). Mean global annual GPP from three satellite-based models using Vc_{max} parameter (PR, BESS, and BEPS) was (132 ± 6) Pg C·a^{-1} (Fig. S10(a)). Mean global annual GPP from four satellite-based models using ε_{max} (MOD17, LRF, EC-LUE, and GLASS) is (114 ± 12) Pg C·a^{-1}, ranging from 98 to 130 Pg C·a^{-1}. Mean global annual GPP from three statistical models (FLUXCOM, NIRv, and GOSIF) were (124 ± 7) Pg C·a^{-1}, (135 ± 9) Pg C·a^{-1}, and (147 ± 16) Pg C·a^{-1}, respectively. Mean global annual GPP from 13 models in the CO_2-inclusive DGVMs ensemble varied substantially, and four of them (CLM5.0, iMAPLE, LPJmL, and LPJwsl) have comparable annual GPP with VPM-v4 (Fig. S10(b)). It is clear that most of the models without biochemical CO_2 effect have lower annual GPP than the models with biochemical CO_2 effect and are noticeably lower than the global GPP estimates from the OCS method.

IAV and trends of global annual GPP from various models are compared (Figs. S11 and S12, Tables S2 and S3 in Appendix A). The global annual GPP from 2000 to 2023 from these models have substantial differences in both IAV and trends over years. We conducted two sets of comparisons to evaluate interannual trends of global annual GPP, based on the data availability among the models. The first comparison covers the period from 2001 to 2011, during which period data from all selected models were available (Figs. 3(c) – (e)) and Table S2). The CO_2-inclusive DGVM ensemble has a large interannual trends of ~0.57 Pg C·a^{-2}. The satellite-based models using Vc_{max} parameter (PR, BESS, and BEPS) have moderate trends ranging from ~0.36 to ~0.46 Pg C·a^{-2}. The CO_2-exclusive DGVM ensemble has a small interannual trend of 0.17 Pg C·a^{-2}. The satellite-based models using ε_{max} parameter have a wide range of interannual trends, with values of 0.89 (VPM-v4), 0.64 (VPM-v3), 0.47 (MOD17), 0.27 (LRF), −0.25 (EC-LUE), and −0.35 (GLASS) Pg C·a^{-2}. The statistical models (FLUXCOM and GOSIF) also have a large range of interannual trends, varying from 0.06 (FLUXCOM) to 0.66 (GOSIF) Pg C a^{-2}. The second comparison covers the period of 2000–2023 (Fig. S13(b) and Table S4 in Appendix A). VPM-v4 (with CO_2) had the largest trend (0.78 Pg C·a^{-2}), followed by VPM-v3 (without CO_2, 0.57 Pg C·a^{-2}), the CO_2-inclusive DGVM ensemble (0.43 Pg C·a^{-2}), and the CO_2-exclusive DGVM ensemble (0.03 Pg C·a^{-2}). The interannual trends of global annual GPP from VPM simulations are consistently larger than those from DGVMs. Among the 13 DGVMs, CO_2-inclusive simulations show large (0.64 Pg C·a^{-2} in iMAPLE) to moderate (0.28 Pg C·a^{-2} in CLASSIC) increasing trend in global annual GPP, while CO_2-exclusive simulations show interannual trends in global annual GPP from small (0.18 Pg C·a^{-2} in LPJmL) increase to a slight decline (−0.04 Pg C·a^{-2} in CABLE-POP).

Journal Pre-proofs

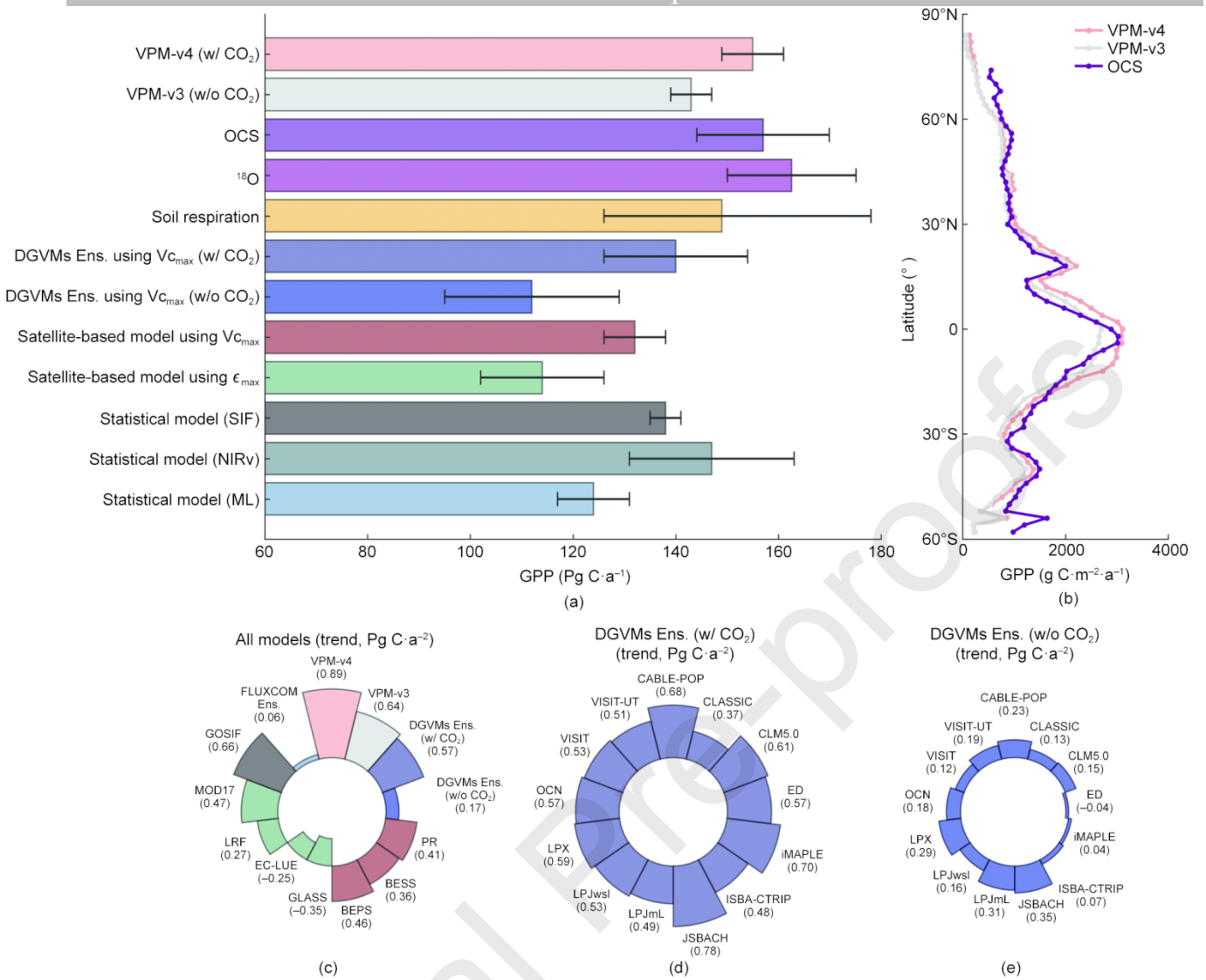


Fig. 3. Intercomparison of GPP estimates from multiple models. (a) Global GPP estimates and their ranges are presented for all models and grouped by category. VPM-v4 and VPM-v3 are the estimates from this study, while estimates for other models are derived from historical literature or published datasets. Detailed estimates for each model can be found in Fig. S10 in Appendix A. The range for each category is calculated across all models within that category using the propagation of uncertainty method. (b) The latitudinal distribution of GPP is shown for VPM-v4, VPM-v3, and the OCS method, with curves estimated as the average of all pixels within each 2° latitudinal band. (c – e) The interannual trends (Pg C·a^{-2}) of the selected models from 2001 to 2011. These models were selected because the data provided by these models overlap during the period of 2001–2011 with (c) the trend of all selected models, and (d, e) are two estimates (CO_2-inclusive, CO_2-exclusive) of the 13 models in DGVM ensemble, respectively.

3.4. Comparison of GPP sensitivity (β_R^{GPP}) to increased CO_2 concentration

We compared the sensitivity of global annual GPP during 2000–2023 from VPM and DGVMs to the increase of c_a (Fig. 4(a)). Global annual GPP from VPM-v4 (slope = 0.90, R^2 = 0.95, $p < 0.01$), the CO_2-inclusive DGVM ensemble (slope = 0.53, R^2 = 0.93, $p < 0.01$), and VPM-v3 (slope = 0.70, R^2 = 0.92, $p < 0.01$) significantly increase with rising c_a. As anticipated, global annual GPP from the CO_2-exclusive DGVM ensemble had little to no changes with rising c_a (slope = 0.04, R^2 = 0.05, p = 0.31). We further calculated a dimensionless coefficient, β_R^{GPP}, to represent the sensitivity of GPP to historical changes in c_a during 2000–2023 (Fig. 4(b) and Table S4). Our method for calculating β_R^{GPP} is based on previous literature and is anticipated to yield a metric that can be directly compared with other studies [19]. The β_R^{GPP} is (0.59 ± 0.16) for the CO_2-inclusive DGVMs and (0.03 ± 0.03) for the CO_2-exclusive DGVMs (Fig. 4(b), Fig. S14 in Appendix A). The β_R^{GPP} is (0.97 ± 0.07) for VPM-v4 and (0.76 ± 0.05) for VPM-v3, respectively (Fig. 4(b)). In both DGVMs and VPM-v4, explicitly including CO_2 substantially enhances the sensitivity of GPP to c_a changes. At the scale of biome, after incorporating the CO_2 into VPM-v4, the sensitivity of annual GPP to c_a increases across all eleven biomes, with the largest increases in EBF (Fig. S15 in Appendix A). The β_R^{GPP} values are large for EBF, moderate for CRO, SAV, and WSA, and small for OSH and WET.

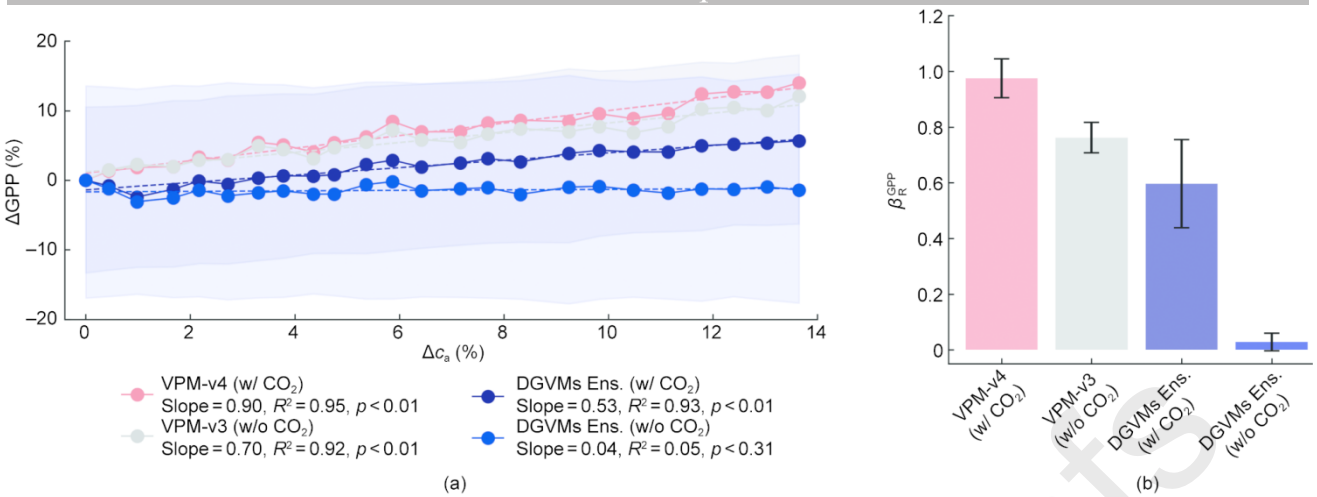


Fig. 4. Sensitivity of GPP to atmospheric CO_2 concentration (c_a). (a) Comparison of the changes in GPP (ΔGPP) against changes in atmospheric CO_2 concentration (Δc_a) using data from both the VPMs (VPM-v4 and VPM-v3) and a DGVM ensemble (CO_2-inclusive and CO_2-exclusive). These two sets of models—yielding four estimates in total—were chosen because they provide continuous global GPP estimates from 2000 to 2023. Slope, R^2, and significance (p) are calculated from simple linear regression. (b) The magnitude and range of the sensitivity coefficient (β_R^{GPP}) for these four estimates. Specific values for each model within the DGVM ensemble can be found in Table S4 and Fig. S14 in Appendix A.

4. Discussion and conclusions

The effects of increased c_a on plants are well recognized but are very difficult to quantify at the ecosystem scale, as it has biochemical effects (e.g., photosynthesis) and biophysical effects (e.g., leaf traits, LAI, and transpiration) [19]. Most satellite-based LUE models use LAI or vegetation indices (e.g., normalized difference vegetation index (NDVI) and EVI) to estimate FPAR, thereby partly accounting for the biophysical CO_2 effect through CO_2-driven increases in canopy leaf area [26,27]. This is evidenced by the fact that, on average, models using remote sensing data (VPM-v3 and GOSIF) have noticeably larger global annual GPP estimates, IAV and trends than those from the CO_2-exclusive DGVM models (ensemble mean and uncertainty of global annual GPP derived from the 13 models: (112 ± 17) Pg C·a^{-1}; Fig. 3(a) and Fig. S10(a)). However, it is also clear that solely incorporation of the biophysical CO_2 effects is not sufficient for accurate GPP estimation [1,2]. Estimates from the 13 DGVM models give an average global GPP of (140 ± 11) Pg C·a^{-1} under CO_2-inclusive scenarios, which is approximately 28 Pg C·a^{-1} (25%) larger than the averaged global GPP under CO_2-exclusive scenarios ((112 ± 17) Pg C·a^{-1}). Therefore, it is imperative to incorporate biochemical CO_2 effects into those satellite-based models using ε_{max} in CO_2 fixation [33].

In this study, we introduced an environmental factor, $f(CO_2)$, to represent the biochemical CO_2 effect in VPM-v4 (Section 2). The spatio – temporal distribution of $f(CO_2)$ reveals that the biochemical CO_2 effect follows a clear spatial pattern, being smaller at high latitudes but larger in tropical and subtropical regions (Fig. S3). This distribution pattern is primarily attributable to the dynamic representation of $\chi(c_i \cdot c_a^{-1})$, which integrates the influences of c_a, air temperature, VPD, and elevation [58]. Previous studies have shown that warm and humid regions typically exhibit a marked CO_2 effect [59]. According to the least-cost hypothesis, when air temperatures are relatively high and water supply is adequate (i.e., when VPD is low), plants can afford to increase or maintain an optimal stomatal aperture [60,61], thereby sustaining higher c_i as c_a rises [18]. This enhances the relative advantage of carboxylation over photorespiration, leading to a more pronounced net CO_2 assimilation [16,18]. Conversely, under conditions of low air temperature or significant drought stress, increases in c_a do not translate into comparable increments in c_i [62,63]. These phenomena have been confirmed by multiple ground-based observational studies [18,28,58,64–66], and help explain the particularly strong biochemical CO_2 effects observed in rainforests, GRA, and SAV ecosystems in the tropical and subtropical regions. Altogether, these results underscore the substantial and non-negligible influence of the biochemical CO_2 effect on photosynthesis at the global scale.

In addition to explicitly modeling both biochemical and biophysical CO_2 effects, VPM-v4 also inherits critical improvements on several environmental and biological factors from VPM-v3 [32]. VPM-v3 considers ① the effect of leaf traits (broadleaf vs needleleaf) on light absorption by chlorophyll [67]; ② plant functional types (C_3 and C_4 photosynthesis pathways) on ε_{max} [23,32]; ③ a site-specific optimum air temperature parameter ($T_{opt\text{-}site}$) on LUE_{max} [31,32,34,68]; and ④ a site-specific water scalar on ε_{max} under dry and normal conditions [32,34]. In comparison to other LUE models that use biome-specific optimum air temperature parameters ($T_{opt\text{-}biome}$) for photosynthesis, these site-specific parameters used in VPM-v3 and VPM-v4 have substantially improved GPP estimates from individual sites to the global level [32].

VPM-v4 incorporates the biochemical CO_2 effect and uses satellite images as input data, representing a major improvement in diagnostic and data-driven TBMs. We selected OCS-derived GPP as a reference because previous research reported that OCS

flux-based GPP correlates well with flux tower observations in tropical regions (e.g., eastern Amazonia), providing a relatively robust estimate of tropical GPP [12]. This consistency highlights the considerable improvement in tropical GPP estimations achieved by VPM-v4. Given the critical role of pan-tropical rainforests in the global carbon cycle and the widespread underestimation of GPP in these regions by most LUE models [22,23,32,53], this improvement is particularly important. The main scientific advance of VPM-v4 is the integration of an explicit, FvCB-based representation of the biochemical CO_2 effect into a satellite-based LUE framework that also represents canopy light absorption from satellite observations. This transparent formulation allows the contribution of the added biochemical pathway to be evaluated through paired VPM-v4 and VPM-v3 simulations under otherwise identical forcing. From a practical perspective, the resulting 2000–2023 global GPP estimates can support analyses of regional and biome-level CO_2 responses, provide prior information for terrestrial-atmospheric carbon-cycle inversions, and offer a complementary reference for the intercomparison and evaluation of TBMs and ESMs.

Many studies have investigated IAV and trends of LAI and vegetation greenness (as measured by NDVI or EVI), using time series from AVHRR data during 1982–2009 [69] and MODIS data since 2000 [70–72]. These satellite records document a continuous increase in vegetation greenness over the global land surface during 2000–2023 [71]. Because VPM-v3, GOSIF, and MOD17 use vegetation indices and/or SIF data, they can capture part of the canopy greenness signal, including the biophysical CO_2 effect, and therefore show moderate increasing trends in global annual GPP even without explicitly incorporating the biochemical CO_2 effect. However, most satellite-based models still exhibit smaller GPP IAV and trends than DGVMs [2,64]. This difference may partly reflect their omission of the biochemical CO_2 effect, although climate variability, land-use change, and disturbances also contribute to differences in modeled GPP variability and trends [3,47,69,73].

The CO_2-exclusive DGVM ensemble has a small interannual trend of 0.17 Pg $C \cdot a^{-2}$ during 2001–2011 (Table S2) and 0.03 Pg $C \cdot a^{-2}$ during 2000–2023 (Table S3), which reflects the increased negative effect of climate changes on GPP in 2010s. The CO_2-inclusive DGVM ensemble has a moderate trend of 0.57 Pg $C \cdot a^{-2}$ during 2001–2011 and 0.43 Pg $C \cdot a^{-2}$ during 2000–2023, which also reflects the increased negative effect of climate change on GPP in 2010s. VPM-v4 reported an interannual trend of 0.89 Pg $C \cdot a^{-2}$ during 2001–2011 and 0.78 Pg $C \cdot a^{-2}$ during 2000–2023. We reviewed the CO_2 sensitivity of GPP (β_R^{GPP}) estimates from previous publications to search for evidence that may support the estimates of the GPP IAV and trends estimated by VPM-v4. Previous publications reported that β_R^{GPP} varies across the studies but generally falls within a relatively moderate range, with estimates of (1.3 ± 2.3) from the ice core measurements of atmospheric O_2 isotopes [74], 1.12 from an analytical framework based on photosynthetic optimization theory at 68 EC tower sites [17], (1.1 ± 0.5) from the satellite-derived evapotranspiration with ecosystem water-use-efficiency models [75], and (0.95 ± 0.2) from the OCS-based methods [76]. VPM-v4 estimates β_R^{GPP} to be 0.97, which falls within the historical estimate range of 0.9 to 1.3 but is higher than 13 models in the CO_2-inclusive DGVM ensemble (0.39 – 0.90, Table S4).

These results should be interpreted alongside other processes and uncertainties. Nutrient limitation and deposition, photosynthetic acclimation to CO_2, and uncertainties in meteorological forcing and satellite data can all modify the biochemical CO_2 effect on GPP. In this context, the CO_2 scalar, $f(CO_2)$, in VPM-v4 should be viewed as an effective net CO_2-related response under current nutrient and acclimation conditions. In the current implementation, $f(CO_2)$ is calculated as a year-specific scalar and applied uniformly to all sub-annual time steps within a given year. This design is consistent with the focus of this study on interannual to multi-decadal changes in GPP, but it does not modify seasonal interactions among CO_2, temperature, water stress, and phenology or the timing and shape of seasonal GPP dynamics. Future work should include more comprehensive uncertainty and sensitivity analyses, develop a temporally varying CO_2 response, and evaluate it against sub-annual EC observations.

As c_a continues to rise, global GPP is expected to increase, especially in tropical regions where the biochemical CO_2 effect is particularly pronounced [77]. Driven by rising c_a and climate change, global greening, as measured by LAI and GPP, was well documented [69]. VPM-v4 predicts a significant increasing interannual trend of global annual GPP over 2000–2023, which is considerably higher than the interannual trends reported in many models. The principal scientific contribution of VPM-v4 is the explicit integration of an FvCB-based biochemical CO_2 response into a satellite-based LUE framework, providing a transparent approach for examining the magnitude and spatial variation of recent GPP change. The resulting 2000 – 2023 global GPP estimates can provide complementary prior information for terrestrial-atmospheric carbon-cycle inversions and a reference for evaluating GPP magnitude and trends in TBMs and ESMs.

Data availability

All datasets used in this study are available. MOD09A1 v6.1 data is available at https://lpdaac.usgs.gov/products/mod09a1v061/. MCD12Q1 v6.1 data is available at https://lpdaac.usgs.gov/products/mcd12q1v061/. ERA5-Land is available at https://cds.climate.copernicus.eu/datasets/reanalysis-era5-land?tab=overview. Atmospheric CO_2 concentration data is available at https://gml.noaa.gov/ccgg/trends/global.html?doi=10.15138/9n0h-zh07. GMTED2010 is available at https://www.usgs.gov/coastal-changes-and-impacts/gmted2010. FLUXNET GPP data is available at

https://fluxnet.org/data/fluxnet2015-dataset/. OCS-derived GPP is available at https://doi.org/10.7298/mxg9-7176. GOSIF GPP is available at https://globalecology.unh.edu/data/GOSIF.html. BESS GPP is available at https://www.environment.snu.ac.kr/data/. BEPS GPP is available at https://www.scidb.cn/en/detail?dataSetId=4d39431492e1481d9c653c140a98d784. DGVMs GPP data is available at https://globalcarbonbudget.org/gcb-2024/. FLUXCOM GPP data is available at https://www.fluxcom.org/. GLASS GPP is available at https://glass.hku.hk/download.html. MODIS GPP is available at https://modis.gsfc.nasa.gov/data/dataprod/mod17.php. GPP estimated from ^{18}O [4], soil respiration [3], NIRv [67], PR [52], EC-LUE [46], and LRF [69] were reported in publications.

Acknowledgment

This study was supported by a research grant from the US National Science Foundation (1946093). We thank the reviewers for their time and effort in reviewing early version of the manuscript. Their comments and suggestions helped improve this manuscript.

References

[1] Ryu Y, Berry JA, Baldocchi DD. What is global photosynthesis? History, uncertainties and opportunities. Remote Sens Environ 2019;223:95–114.
[2] Anav A, Friedlingstein P, Beer C, Ciais P, Harper A, Jones C, et al. Spatiotemporal patterns of terrestrial gross primary production: a review. Rev Geophys 2015;53(3):785–818.
[3] Beer C, Reichstein M, Tomelleri E, Ciais P, Jung M, Carvalhais N, et al. Terrestrial gross carbon dioxide uptake: global distribution and covariation with climate. Science 2010;329(5993):834–8.
[4] Ciais P, Sabine C, Bala G, Bopp L, Brovkin V, Canadell J, et al. Carbon and other biogeochemical cycles. In: Stocker TF, Qin D, Plattner GK, Tignor M, Allen SK, Boschung J, et al., editors. Climate change 2013—the physical science basis: contribution of Working Group I to the Fifth Assessment Report of the Intergovernmental Panel on Climate Change. Cambridge: Cambridge University Press; 2014. p. 465–570.
[5] Gampe D, Zscheischler J, Reichstein M, O'Sullivan M, Smith WK, Sitch S, et al. Increasing impact of warm droughts on northern ecosystem productivity over recent decades. Nat Clim Chang 2023;13(11):1272.
[6] Monteith JL. Solar radiation and productivity in tropical ecosystems. J Appl Ecol 1972;9(3):747–66.
[7] Jung M, Koirala S, Weber U, Ichii K, Gans F, Camps-Valls G, et al. The FLUXCOM ensemble of global land‐atmosphere energy fluxes. Sci Data 2019;6(1):74.
[8] Guanter L, Zhang Y, Jung M, Joiner J, Voigt M, Berry JA, et al. Global and time-resolved monitoring of crop photosynthesis with chlorophyll fluorescence. Proc Natl Acad Sci USA 2014;111(14):E1327–33.
[9] Sitch S, Smith B, Prentice IC, Arneth A, Bondeau A, Cramer W, et al. Evaluation of ecosystem dynamics, plant geography and terrestrial carbon cycling in the LPJ dynamic global vegetation model. Glob Change Biol 2003;9(2):161–85.
[10] Li B, Ryu Y, Jiang C, Dechant B, Liu J, Yan Y, et al. BESSv2.0: a satellite-based and coupled-process model for quantifying long-term global land–atmosphere fluxes. Remote Sens Environ 2023;295:113696.
[11] Leng J, Chen JM, Li W, Luo X, Xu M, Liu J, et al. Global datasets of hourly carbon and water fluxes simulated using a satellite-based process model with dynamic parameterizations. Earth Syst Sci Data 2024;16(3):1283–300.
[12] Lai J, Kooijmans LMJ, Sun W, Lombardozzi D, Campbell JE, Gu L, et al. Terrestrial photosynthesis inferred from plant carbonyl sulfide uptake. Nature 2024;634(8035):855–61.
[13] Jian J, Bailey V, Dorheim K, Konings AG, Hao D, Shiklomanov AN, et al. Historically inconsistent productivity and respiration fluxes in the global terrestrial carbon cycle. Nat Commun 2022;13(1):1733.
[14] Welp LR, Keeling RF, Meijer HAJ, Bollenbacher AF, Piper SC, Yoshimura K, et al. Interannual variability in the oxygen isotopes of atmospheric CO_2 driven by El Niño. Nature 2011;477(7366):579–82.
[15] Sellers PJ. Canopy reflectance, photosynthesis and transpiration. Int J Remote Sens 1985;6(8):1335–72.
[16] Farquhar GD, von Caemmerer S, Berry JA. A biochemical model of photosynthetic CO_2 assimilation in leaves of C_3 species. Planta 1980,149(1):78–90.
[17] Chen C, Riley WJ, Prentice IC, Keenan TF. CO_2 fertilization of terrestrial photosynthesis inferred from site to global scales. Proc Natl Acad Sci USA 2022;119(10):e2115627119.
[18] Ainsworth EA, Rogers A. The response of photosynthesis and stomatal conductance to rising [CO_2]: mechanisms and environmental interactions. Plant Cell Environ 2007;30(3):258–70.
[19] Keenan TF, Luo X, Stocker BD, De Kauwe MG, Medlyn BE, Prentice IC, et al. A constraint on historic growth in global photosynthesis due to rising CO_2. Nat Clim Chang 2023;13(12):1376–81.
[20] Monteith JL. Climate and the efficiency of crop production in Britain. Philos Trans R Soc Lond B Biol Sci 1977;281(980):277–94.
[21] De Kauwe MG, Keenan TF, Medlyn BE, Prentice IC, Terrer C. Satellite based estimates underestimate the effect of CO_2 fertilization on net primary productivity. Nat Clim Chang 2016;6(10):892–3.
[22] Running SW, Nemani RR, Heinsch FA, Zhao M, Reeves M, Hashimoto H. A continuous satellite-derived measure of global terrestrial primary production. Bioscience 2004;54(6):547–60.
[23] Zhang Y, Xiao X, Wu X, Zhou S, Zhang G, Qin Y, et al. A global moderate resolution dataset of gross primary production of vegetation for 2000-2016. Sci Data 2021;8(1):67.
[24] Li X, Xiao J. Mapping photosynthesis solely from solar-induced chlorophyll fluorescence: a global, fine-resolution dataset of gross primary production derived from OCO-2. Remote Sens 2019;11(21):2563.
[25] Zhang-Zheng H, Adu-Bredu S, Duah-Gyamfi A, Moore S, Addo-Danso SD, Amissah L, et al. Contrasting carbon cycle along tropical forest aridity gradients in west Africa and Amazonia. Nat Commun 2024;15(1):3158.
[26] Keenan TF, Hollinger DY, Bohrer G, Dragoni D, Munger JW, Schmid HP, et al. Increase in forest water-use efficiency as atmospheric carbon dioxide concentrations rise. Nature 2013;499(7458):324–7.
[27] Donohue RJ, Roderick ML, McVicar TR, Farquhar GD. Impact of CO_2 fertilization on maximum foliage cover across the globe's warm, arid environments. Geophys Res Lett 2013;40(12):3031–5.

[28] Sun Z, Wang X, Zhang X, Tani H, Guo E, Yin S, et al. Evaluating and comparing remote sensing terrestrial GPP models for their response to climate variability and CO_2 trends. Sci Total Environ 2019;668:696–713.
[29] Walker AP, De Kauwe MG, Bastos A, Belmecheri S, Georgiou K, Keeling RF, et al. Integrating the evidence for a terrestrial carbon sink caused by increasing atmospheric CO_2. New Phytol 2021;229(5):2413–45.
[30] Kolby Smith W, Reed SC, Cleveland CC, Ballantyne AP, Anderegg WRL, Wieder WR, et al. Large divergence of satellite and Earth system model estimates of global terrestrial CO_2 fertilization. Nat Clim Chang 2016;6(3):306–10.
[31] Pan L, Xiao X, Pan B, Meng C, Staebler RM, Zhang C, et al. Interannual variations and trends of gross primary production and transpiration of four mature deciduous broadleaf forest sites during 2000–2020. Remote Sens Environ 2024;304:114042.
[32] Pan L, Xiao X, Pan B, Meng C, Doughty R, Qin Y, et al. Vegetation Photosynthesis Model v3.0: improved estimates of terrestrial gross primary production from individual eddy flux tower sites to the globe. J Remote Sens 2025;5:0471.
[33] Prentice IC, Balzarolo M, Bloomfield KJ, Chen JM, Dechant B, Ghent D, et al. Principles for satellite monitoring of vegetation carbon uptake. Nat Rev Earth Environ 2024;5(11):818-32.
[34] Meng C, Xiao X, Pan L, Pan B, Scott RL, Wagle P, et al. Interannual variability and trends of gross primary production and transpiration in savannas and grasslands from 2000 to 2021. Front Earth Sci 2025;19(2):246-60.
[35] Vermote E. MODIS/Terra surface reflectance 8-day L3 global 500m SIN grid V061 [dataset]. Sioux Falls: NASA EOSDIS Land Processes Distributed Active Archive Center; 2021.
[36] Frey RA, Ackerman SA, Liu Y, Strabala KI, Zhang H, Key JR, et al. Cloud detection with MODIS. Part I: improvements in the MODIS cloud mask for collection 5. J Atmos Ocean Technol 2008;25(7):1057–72.
[37] Jensen JR. Remote sensing of the environment: an earth resource perspective. 2nd ed. New Delhi: Pearson Education India; 2009.
[38] Sulla-Menashe D, Friedl MA. User guide to collection 6 MODIS land cover (MCD12Q1 and MCD12C1) product. Report. Reston: U.S. Geological Survey; 2018.
[39] Copernicus Climate Change Service (C3S). ERA5-Land hourly data from 1950 to present [dataset]. Reading: Copernicus Climate Change Service (C3S) Climate Data Store (CDS); 2019.
[40] Muñoz-Sabater J, Dutra E, Agustí-Panareda A, Albergel C, Arduini G, Balsamo G, et al. ERA5-Land: a state-of-the-art global reanalysis dataset for land applications. Earth Syst Sci Data 2021;13(9):4349–83.
[41] Meek DW, Hatfield JL, Howell TA, Idso SB, Reginato RJ. A generalized relationship between photosynthetically active radiation and solar radiation. Agron J 1984;76(6):939–45.
[42] Ma X, Huete A, Yu Q, Restrepo-Coupe N, Beringer J, Hutley LB, et al. Parameterization of an ecosystem light-use-efficiency model for predicting savanna GPP using MODIS EVI. Remote Sens Environ 2014;154:253–71.
[43] Dye DG. Spectral composition and quanta-to-energy ratio of diffuse photosynthetically active radiation under diverse cloud conditions. J Geophys Res Atmos 2004;109(D10):203.
[44] Lan X, Tans P, Thoning KW. Trends in globally-averaged CO_2 determined from NOAA Global Monitoring Laboratory measurements [dataset]. Boulder: NOAA Global Monitoring Laboratory; 2025.
[45] Danielson JJ, Gesch DB. Global multi-resolution terrain elevation data 2010 (GMTED2010). Report. Reston: U.S. Geological Survey; 2011. Report No.: 2011–1073.
[46] Sitch S, Friedlingstein P, Gruber N, Jones SD, Murray-Tortarolo G, Ahlström A, et al. Recent trends and drivers of regional sources and sinks of carbon dioxide. Biogeosciences 2015;12(3):653–79.
[47] Keenan TF, Prentice IC, Canadell JG, Williams CA, Wang H, Raupach M, et al. Recent pause in the growth rate of atmospheric CO_2 due to enhanced terrestrial carbon uptake. Nat Commun 2017;8:16137.
[48] Badgley G, Anderegg LDL, Berry JA, Field CB. Terrestrial gross primary production: Using NIR_V to scale from site to globe. Glob Change Biol 2019;25(11):3731–40.
[49] Tramontana G, Jung M, Schwalm CR, Ichii K, Camps-Valls G, Ráduly B, et al. Predicting carbon dioxide and energy fluxes across global FLUXNET sites with regression algorithms. Biogeosciences 2016;13(14):4291–313.
[50] Liang S, Cheng J, Jia K, Jiang B, Liu Q, Xiao Z, et al. The Global Land Surface Satellite (GLASS) product suite. Bull Am Meteorol Soc 2021;102(2):E323–37.
[51] Tagesson T, Tian F, Schurgers G, Horion S, Scholes R, Ahlström A, et al. A physiology-based Earth observation model indicates stagnation in the global gross primary production during recent decades. Glob Change Biol 2021;27(4):836–54.
[52] Zhao M, Heinsch FA, Nemani RR, Running SW. Improvements of the MODIS terrestrial gross and net primary production global data set. Remote Sens Environ 2005;95(2):164–76.
[53] Zheng Y, Shen R, Wang Y, Li X, Liu S, Liang S, et al. Improved estimate of global gross primary production for reproducing its long-term variation, 1982–2017. Earth Syst Sci Data 2020;12(4):2725–46.
[54] Xiao X. Light absorption by leaf chlorophyll and maximum light use efficiency. IEEE Trans Geosci Remote Sens 2006;44(7):1933–5.
[55] Pan L, Xiao X, Yao Y, Pan B, Yin C, Meng C, et al. Site-specific apparent optimum air temperature for vegetation photosynthesis across the globe. Sci Data 2024;11(1):758.
[56] Baig S, Medlyn BE, Mercado LM, Zaehle S. Does the growth response of woody plants to elevated CO_2 increase with temperature? A model-oriented meta-analysis. Glob Change Biol 2015;21(12):4303–19.
[57] Friedlingstein P, O'Sullivan M, Jones MW, Andrew RM, Hauck J, Landschützer P, et al. Global carbon budget 2024. Earth Syst Sci Data 2025;17(3):965–1039.
[58] Wang H, Prentice IC, Keenan TF, Davis TW, Wright IJ, Cornwell WK, et al. Towards a universal model for carbon dioxide uptake by plants. Nat Plants 2017;3(9):734–41.
[59] Piao S, Wang X, Park T, Chen C, Lian X, He Y, et al. Characteristics, drivers and feedbacks of global greening. Nat Rev Earth Environ 2020;1(1):14–27.
[60] Medlyn BE, Duursma RA, Eamus D, Ellsworth DS, Prentice C, Barton CM, et al. Reconciling the optimal and empirical approaches to modelling stomatal conductance. Glob Chang Biol 2012;18(11):3476.
[61] Prentice IC, Dong N, Gleason SM, Maire V, Wright IJ. Balancing the costs of carbon gain and water transport: testing a new theoretical framework for plant functional ecology. Ecol Lett 2014;17(1):82–91.
[62] Chaves MM, Flexas J, Pinheiro C. Photosynthesis under drought and salt stress: Regulation mechanisms from whole plant to cell. Ann Bot 2009;103(4):551–60.
[63] Sage RF, Kubien DS. The temperature response of C_3 and C_4 photosynthesis. Plant Cell Environ 2007;30(9):1086–106.
[64] Piao S, Sitch S, Ciais P, Friedlingstein P, Peylin P, Wang X, et al. Evaluation of terrestrial carbon cycle models for their response to climate variability and to CO_2 trends. Glob Change Biol 2013;19(7):2117–32.

[65] Farquhar GD, Sharkey TD. Stomatal conductance and photosynthesis. Annu Rev Plant Physiol 1982;33(1):317–45.
[66] Collatz GJ, Ball JT, Grivet C, Berry JA. Physiological and environmental regulation of stomatal conductance, photosynthesis and transpiration: a model that includes a laminar boundary layer. Agric For Meteorol 1991;54(2–4):107–36.
[67] Pan B, Xiao X, Pan L, Meng C, Blanken PD, Burns SP, et al. Incorporation of needleleaf traits improves estimation of light absorption and gross primary production of evergreen needleleaf forests. Agric For Meteorol 2025;368:110526.
[68] Chang Q, Xiao X, Doughty R, Wu X, Jiao W, Qin Y. Assessing variability of optimum air temperature for photosynthesis across site-years, sites and biomes and their effects on photosynthesis estimation. Agric For Meteorol 2021;298–299:108277.
[69] Zhu Z, Piao S, Myneni RB, Huang M, Zeng Z, Canadell JG, et al. Greening of the Earth and its drivers. Nat Clim Chang 2016;6(8):791–5.
[70] Chen C, Park T, Wang X, Piao S, Xu B, Chaturvedi RK, et al. China and India lead in greening of the world through land-use management. Nat Sustain 2019;2(2):122–9.
[71] Gui Y, Wang K, Huntingford C, Wei S, Li X, Myneni RB, et al. Vegetation greenness in 2024. Nat Rev Earth Environ 2025;6(4):255–7.
[72] Li X, Wang K, Huntingford C, Zhu Z, Peñuelas J, Myneni RB, et al. Vegetation greenness in 2023. Nat Rev Earth Environ 2024;5(4):241–3.
[73] Kurz WA, Dymond CC, Stinson G, Rampley GJ, Neilson ET, Carroll AL, et al. Mountain pine beetle and forest carbon feedback to climate change. Nature 2008;452(7190):987–90.
[74] Ciais P, Tagliabue A, Cuntz M, Bopp L, Scholze M, Hoffmann G, et al. Large inert carbon pool in the terrestrial biosphere during the Last Glacial Maximum. Nat Geosci 2012;5(1):74–9.
[75] Cheng L, Zhang L, Wang YP, Canadell JG, Chiew FHS, Beringer J, et al. Recent increases in terrestrial carbon uptake at little cost to the water cycle. Nat Commun 2017;8(1):110.
[76] Campbell JE, Berry JA, Seibt U, Smith SJ, Montzka SA, Launois T, et al. Large historical growth in global terrestrial gross primary production. Nature 2017;544(7648):84–7.
[77] Huntingford C, Zelazowski P, Galbraith D, Mercado LM, Sitch S, Fisher R, et al. Simulated resilience of tropical rainforests to CO_2-induced climate change. Nat Geosci 2013;6(4):268–73.

Competing interests

The authors declare that they have no competing interests.

Journal Pre-proofs